JTTEE5 16:512–523
DOI: 10.1007/s11666-007-9073-0
1059-9630/$19.00 © ASM International

Peer Reviewed

Clogging and Lump Formation During Atmospheric Plasma Spraying with Powder Injection Downstream the Plasma Gun

Isabelle Choquet, Stefan Björklund, Jimmy Johansson, and Jan Wigren

(Submitted October 8, 2006; in revised form June 26, 2007)

This study aimed to numerically and experimentally investigate lump formation during atmospheric plasma spraying with powder injection downstream the plasma gun exit. A first set of investigations was focused on the location and orientation of the powder port injector. It turned out impossible to keep the coating quality while avoiding lumps by simply moving the powder injector. A new geometry of the powder port ring holder was designed and optimized to prevent nozzle clogging, and lump formation using a gas screen. This solution was successfully tested for applications with Ni-5wt.%Al and ZrO_2-7wt.%Y_2O_3 powders used in production. The possible secondary effect of plasma jet shrouding by the gas screen, and its consequence on powder particles prior to impact was also studied.

Keywords influence of spray parameters, shrouded spraying, spray deposition

1. Introduction

During atmospheric plasma spraying (APS), powder is injected into a plasma jet, melted, and deposited onto a substrate. Techniques for particle injection may differ in the angle with respect to the axis of the jet, and the location of injection: upstream or downstream the nozzle outlet, i.e., inside or outside the anode constriction region. In this study, the powder is injected into the plasma jet at a short distance downstream the nozzle exit, as illustrated in Fig. 1a-b.

This study has been motivated by a problem met in production, under standard operation conditions (specified later on) defining our framework. It has been observed that a back-stream of powder may return to the spray gun, leading to clogging of the nozzle wall (Fig. 1a-b), and lumps in the coating (Fig. 2). A dramatic raise of clogging frequency can occur (Ref 1) under certain operation conditions when increasing the carrier gas flow rate above some limit. When clogging occurs during spraying, the powder clogged on the nozzle or on the end piece of the spray gun becomes liquid due to the high wall temperature and aggregates in larger droplets. The droplets are pulled by gravity as in Fig. 1b, get loose and may fall into the plasma jet. In that case, they cause disturbances in the spraying process resulting in blisters and lumps in the coating (Fig. 2). Blisters and lumps are much larger than unmelted, by a factor 10 or so. As such coating defects are unacceptable, the damaged work-piece must be stripped and recoated. Lump formation in production thus results in important wastes in terms of powder particles, energy and time.

This study resumes previous investigations (Ref 2, 3) aiming at developing a simple solution for avoiding lump formation, while preserving the desired coating properties. Both numerical simulations using the Fluent CFD software (Lebanon, NH), and experimental observations and measurements were carried out.

The framework is presented in section 2. The main aspects of the numerical model, including computational domain and mesh, plasma fluid, and powder particle models, are given in section 3. Test cases have been simulated numerically to investigate the effect of parameters such as carrier gas flow rate or powder port location on particle backflow toward the nozzle wall. They are discussed in section 4 and 4.1. Details about the gas screen proposed to prevent powder particles flowing backward from reaching the nozzle wall are given in section 4.2. Numerical test cases intended to investigate the gas screen effect on the plasma jet and the powder particles are discussed in sections 4.3, 4.4. These simulations are supplemented by experimental results in section 5 to characterize the powder particles prior to impact on the substrate, and the coating properties.

2. Framework

All calculations and testing were conducted using the F4 atmospheric plasma spray gun manufactured by Sulzer Metco AG (Wohlen, Switzerland). Its gas injector has injection holes in the tangential direction, resulting in a continuous motion of the arc root attachment, and causing

Isabelle Choquet and **Stefan Björklund,** Department TMD, University West, Box 957, SE-461 29, Trollhättan, Sweden; **Jimmy Johansson** and **Jan Wigren,** Volvo Aero Corporation, Trollhättan, Sweden. Contact e-mail: isabelle.choquet@hv.se.

Nomenclature

Latin notations

c_p	specific heat capacity of the powder particle, J kg^{-1} K^{-1}
$C_{1\varepsilon}$, $C_{2\varepsilon}$, C_μ	constants of the RNG k-ε model, dimensionless
$D_{i,m}$	diffusion coefficient of species i in the mixture, m^2 s^{-1}
e_T	total specific energy of the fluid $e_T = h - p\rho^{-1} + 1/2u^2$, J kg^{-1}
$\vec{F}_{ext}$	external forces applied on the fluid, N m^{-3}
G_k	rate of turbulent kinetic energy generated by velocity gradients, kg m^{-1} s^{-3}
h	specific enthalpy of the fluid $h = \sum Y_i h_i$, J kg^{-1}
h_i	specific enthalpy of the species i, J kg^{-1}
$\vec{J}_i$	diffusion flux of species i in the mixture, kg m^{-2} s^{-1}
k	turbulent kinetic energy, m^2 s^{-2}
p	static pressure of the fluid, Pa
Pr_t	turbulent Prandtl number
r	radial position (at nozzle outlet), m
r_0	nozzle radius at the plasma gun exit, m
R_ε	rate of dissipation rate ε generated by rapid strain and streamline curvature, kg m^{-1} s^{-4}
S_{swirl}	ratio between the flux of angular and of axial momentum, or swirl coefficient
S_e	energy source term due to the interaction between fluid and powder particles, J kg^{-1}
S_m	mass source term due to the interaction between fluid and powder particles, kg m^{-3} s^{-1}
Sc_t	turbulent Schmidt number
T	temperature of the fluid, K
T_{max}	maximum temperature T (at nozzle outlet), K
T_{melt}	melting temperature of the powder particle, K
T_{wall}	wall temperature, K
u	velocity norm of the fluid, m s^{-1}
$\vec{u}$	velocity vector of the fluid, m s^{-1}
u_{max}	maximum velocity norm (at nozzle outlet), m s^{-1}
Y_i	mass fraction of species i

Greek notations

α_k	inverse effective Prandtl number for the turbulent kinetic energy k
α_ε	inverse effective Prandtl number for the turbulent dissipation rate ε
Δh_{melt}	latent heat of fusion of the powder particle, J kg^{-1}
ε	dissipation rate of turbulent kinetic energy, m^2 s^{-3}
κ	laminar thermal conductivity of the fluid, W m^{-1} K^{-1}
κ_t	turbulent thermal conductivity of the fluid, W m^{-1} K^{-1}
κ_{eff}	effective thermal conductivity of the fluid $\kappa_{eff} = \kappa_t + \kappa$, W m^{-1} K^{-1}
κ_p	thermal conductivity of the powder particle, W m^{-1} K^{-1}
μ	laminar dynamic viscosity, kg m^{-1} s^{-1}
μ_t	turbulent dynamic viscosity, kg m^{-1} s^{-1}
μ_{eff}	effective dynamic viscosity $\mu_{eff} = \mu_t + \mu$, kg m^{-1} s^{-1}
ρ	density of the fluid, kg m^{-3}
ρ_p	density of the powder particle, kg m^{-3}
$\bar{\bar{\tau}}$	laminar viscous stress tensor, kg m^{-1} s^{-2}
$\bar{\bar{\tau}}_t$	Reynolds stress tensor, kg m^{-1} s^{-2}
$\bar{\bar{\tau}}_{eff}$	effective stress tensor $\bar{\bar{\tau}}_{eff} = \bar{\bar{\tau}}_t + \bar{\bar{\tau}}$, kg m^{-1} s^{-2}

Mathematical symbols

$\bar{\bar{I}}$	unit tensor
∂_t	partial derivative with respect to time
$\otimes$	tensorial product
$\nabla\cdot$	divergence operator
$\vec{\nabla}$	gradient operator

a swirl of the plasma jet. This spray gun is equipped with a Sulzer Metco annular holder ring with one or two threads for assembly of up to two powder injectors. Powder feed rates can reach up to 90 g/min.

The parameters defining the anode diameter and the injector positioning retained in this study are summarized in Table 1, and the related spray conditions used in production are given in Table 2. All sprayings were done in air at standard atmospheric conditions.

The two powders used were spherical with rather broad distribution in size as supplied:

(a) Ni-5wt.%Al Amdry 956 from Sulzer Metco (Volvo Aero PM 819-37) characterized by the size distribution of Table 3, and sprayed to form the bond coat.

(b) ZrO_2-7wt.%Y_2O_3 Amperit 827.873 from HC Starck (Volvo Aero PM 819-20) characterized by the size distribution reported Table 4, and used to make the top coat.

It was observed numerically (see section 4) and experimentally that the powder back-stream initiating lump formation is mainly made of small particles. Lump formation could thus be avoided doing a sifting of the powder to remove the smallest particles causing clogging. However, this solution was not retained because of the resultant increase in production costs.

As can be seen in Tables 3 and 4, the size distributions were provided over rather broad size intervals, while knowledge about small particles was an important issue in this study. To better describe the questioned particles, powder samples were sifted to eliminate particles of diameter larger than 50 μm, and the remaining sets were scanned. The corresponding data are reported in Fig. 3a

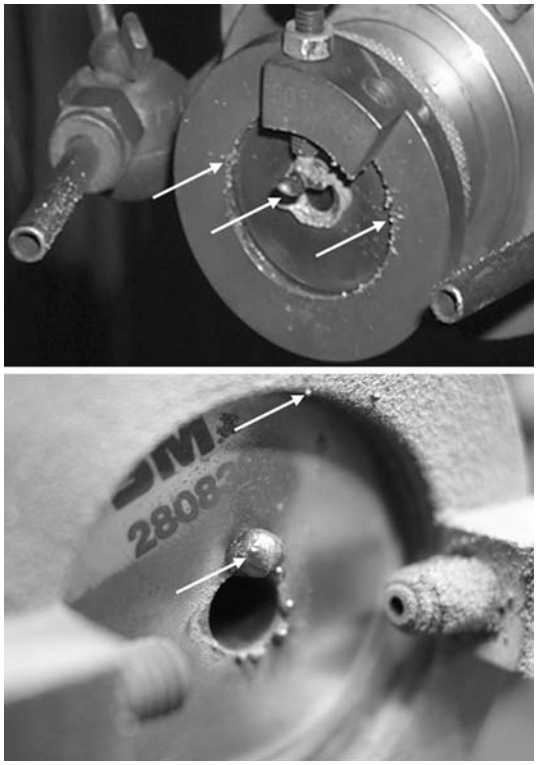

Fig. 1 Photograph of a plasma gun after spraying (F4 by Sulzer Metco). Traces of clogging on the nozzle wall and powder port ring holder are pointed by arrows. Top: with one powder injector, Bottom: with two powder injectors

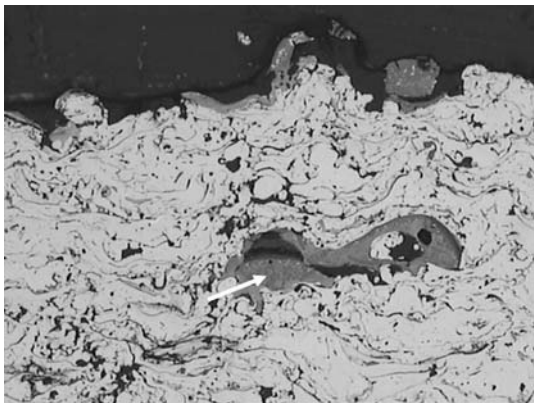

Fig. 2 Optical microphotographs (768×576 μm), microstructure of a ZrO_2-7wt.%Y_2O_3 top coat containing lumps

and b; notice that the percentage in weight in these figures refers to the subset of particles with diameter less than 50 μm rather than the complete powder lot. The minimum diameter observed was about 15 μm for Ni-5wt.%Al and 5 μm for ZrO_2-7wt.%Y_2O_3. These data have been used to characterize the set of Ni-5wt.%Al (ZrO_2-7wt.%Y_2O_3) particles when simulating the powder heating and acceleration by the plasma jet (see section 3.3 for further details).

Table 1 Geometry

Test case	A	B
Nozzle internal diameter, mm	6	8
Ring external diameter, mm	25	25
Powder hose length, m	5	5
Powder injector diameter, mm	1.8	2
Powder injector exit location:		
Horizontal—or jet—axis, mm	5	5
Vertical axis, mm	6	7
Powder port angle, °	90	90
Spray distance, mm	120	120

Table 2 Thermal spray parameters

Test case	A	B
Primary gas: argon, slpm	40	40
Secondary gas: hydrogen, slpm	13	12
Gun voltage, V	63-75	60-72
Gun amperage, A	600	640
Thermal efficiency, %	55	55
Carrier gas: argon, slpm	4	3.3
Powder	Ni-5wt.%Al	ZrO_2-7wt.%Y_2O_3
Powder feed rate, g/min	54	90

Table 3 Ni-5wt.%Al size distribution (sieve analysis)

Diameter (μm)	<45	45-90	90-125	>125
% in weight	1.9	96.9	1.2	0.

Table 4 ZrO_2-7wt.%Y_2O_3 size distribution (sieve analysis)

Diameter (μm)	<45	45-75	75-106	>106
% in weight	45.8	46.5	7.0	0.7

3. Numerical Model

APS processes are composed of three subprocesses: the plasma generation by an arc discharge, the plasma/powder particle interaction, and the coating formation. Computations made in this study focused on the plasma/powder particle interaction, using the simulation software Fluent (versions 6.1 and 6.2).

3.1 Mesh

The computational domain was 3-dimensional and started from the nozzle wall at the exit of the plasma gun (left hand side of Fig. 4). It included the powder port ring holder fixed at the nozzle outlet (photographs in Fig. 1). The domain ended at the substrate location without accounting for the substrate wall. Its radial extension was taken slightly larger than six-nozzle radius since the plasma jet expands when flowing away from the nozzle and the domain must be large enough for imposing valid boundary conditions on its radial periphery. The geometrical dimensions are reported in Table 1.

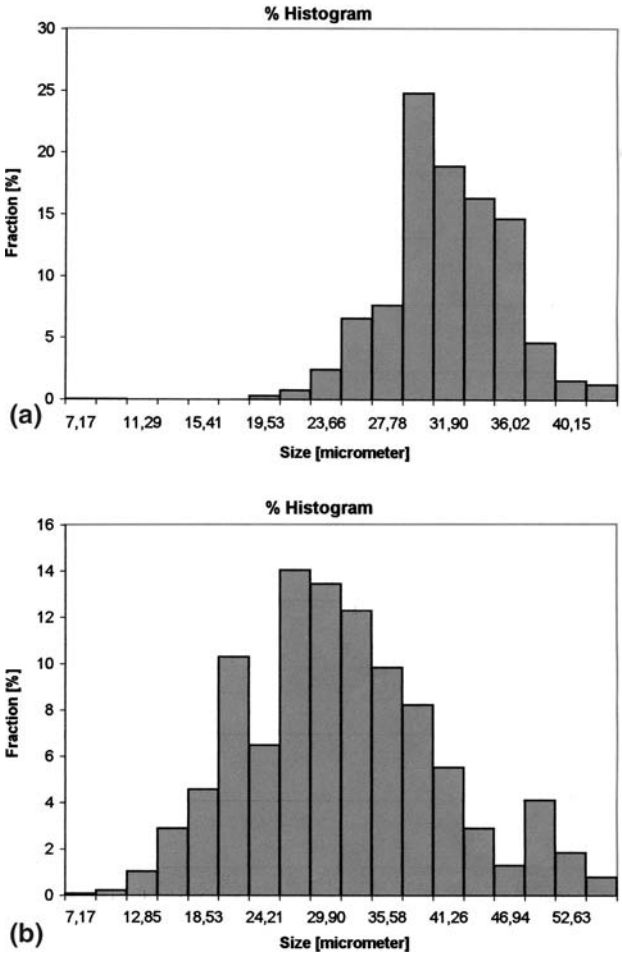

Fig. 3 (a) Detailed size distribution for the subset of Ni-5wt.%Al particles with diameter less than 50 μm, scan analysis. (b) Detailed size distribution for the subset of ZrO_2-7wt.%Y_2O_3 particles with diameter less than 50 μm, scan analysis

The meshes, optimized for the various investigated powder port holder rings, were made of hexahedrons except in the gas screen channels and in the vicinity of the nozzle wall outside the plasma jet (where hexahedrons were combined with tetrahedrons). They were as usual more refined in the plasma jet, and in the mixing zone between plasma-jet and surrounding air. In addition, they were also carefully refined in the vicinity of the nozzle wall and the powder injector, in order to better capture the small variations of the flow field (such as weak turbulent effects) and the trajectories of the powder particles flowing backward. As an illustration, a mesh made of 4,143,960 grid cells was used for calculating the results discussed in section 4.3.

3.2 Fluid Model

The fluid was assumed compressible as the maximum Mach number associated with the plasma jet was about 1.5 and 0.5 for test case A and B, respectively. Among the sources of instability met in plasma spray, it is known

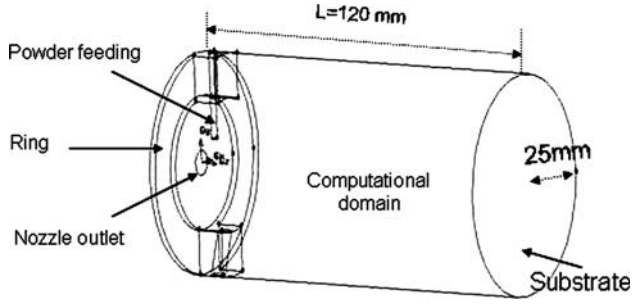

Fig. 4 Computational domain

(Ref 4) that arc root fluctuations have a lower time scale (from 0.5 to 0.05 ms) than the residence time of powder particles in the plasma jet (about 1 ms). Although these fluctuations could affect the particle trajectories, they have not been considered in this study. As Kelvin-Helmholtz vortices were expected to be generated in the plasma-air mixing layer (Ref 5-6), the flow was assumed turbulent. A viscous model was thus used jointly with the Reynolds decomposition, and the Boussinesq hypothesis. Notice that for a variable-density flow the resulting system of equations, given bellow, can be interpreted as Favre-averaged Navier-Stokes equations with the velocities representing mass-averaged values (Ref 7). Three different species ($i = 1, 2, 3$) were taken into account: the plasma gas, the surrounding air, and the carrier gas. The plasma gas was formed by an ionized mixture of primary gas (argon) and secondary gas (hydrogen); the proportions are given in Table 2. The carrier gas was pure argon. Each species was supposed to be in local thermal and chemical equilibrium. Their thermodynamic properties and laminar transport coefficients were calculated based on the temperature dependent data derived from kinetic theory in (Ref 8). The related fluid properties were calculated using mixing laws. Notice that the fluctuations of the transport coefficients (caused by turbulence) were neglected. The species and fluid flow were thus governed by the following set of compressible and Reynolds-averaged turbulent Navier-Stokes equations:

$$\partial_t(\rho Y_i) + \nabla \cdot (\rho Y_i \vec{u}) = -\nabla \cdot \vec{J}_i \quad i = 1, 2$$

$$\partial_t \rho + \nabla \cdot (\rho \vec{u}) = S_m$$

$$\partial_t(\rho \vec{u}) + \nabla \cdot (\rho \vec{u} \otimes \vec{u}) = -\overrightarrow{\nabla} p + \nabla \cdot \overline{\overline{\tau}}_{eff} + \vec{F}_{ext}$$

$$\partial_t(\rho e_T) + \nabla \cdot [\vec{u}(\rho e_T + p)] = \nabla \cdot \left[\kappa_{eff} \overrightarrow{\nabla} T + \overline{\overline{\tau}}_{eff} \cdot \vec{u} - \sum_{i=1}^{3} h_i \vec{J}_i \right] + S_e$$

The diffusion flux $\vec{J}_i = -\left(\rho D_{i,m} + \mu_t S c_t^{-1}\right) \overrightarrow{\nabla} Y_i$ of species i, due to concentration gradients in the mixture, results in a source term in the i-species transport equation and in the energy conservation equation through the enthalpy flux $h_i \vec{J}_i$. The effect of external forces $\vec{F}_{ext}$ on the fluid, such as gravitation, was neglected. The mass and energy source terms due to the interaction with the dispersed phase (powder particles) were set to $S_m = 0$ and $S_e = 0$ when neglecting loading effects. The laminar stress tensor was

defined applying Stokes relation to an isotropic and Newtonian fluid: $\overline{\overline{\tau}} = \mu\left(\vec{\nabla}\vec{u} + \vec{\nabla}\vec{u}^{T}\right) - {}^{2}/_{3}\mu\nabla\cdot\left(\vec{u}\overline{\overline{I}}\right)$. The turbulence stress tensor $\overline{\overline{\tau}}_t$ and heat flux $\kappa_t\vec{\nabla}T$ were defined by analogy to the laminar terms applying the Boussinesq closure assumption: $\overline{\overline{\tau}}_t = \mu_t\left(\vec{\nabla}\vec{u} + \vec{\nabla}\vec{u}^{T}\right) - \frac{2}{3}\left(\rho k\overline{\overline{I}} + \mu_t\nabla\cdot\left(\vec{u}\overline{\overline{I}}\right)\right)$, where $\mu_t = \rho C_\mu k^2\varepsilon^{-1}$ and $\kappa_t = \mu_t\,\mathrm{Pr}_t^{-1}$.

This system was closed by the ideal gas law and a k-ε model in its RNG formulation (that can account for the effect of swirl on turbulence). The turbulent kinetic energy k and its dissipation rate ε were thus governed by

$$\partial_t(\rho k) + \nabla\cdot(\rho k\vec{u}) = \nabla\cdot\left(\alpha_k\mu_{\mathrm{eff}}\vec{\nabla}k\right) + G_k - \rho\varepsilon$$

$$\partial_t(\rho\varepsilon) + \nabla\cdot(\rho\varepsilon\vec{u}) = \nabla\cdot\left(\alpha_\varepsilon\mu_{\mathrm{eff}}\vec{\nabla}\varepsilon\right) + C_{1\varepsilon}G_k\frac{\varepsilon}{k} - C_{2\varepsilon}\rho\frac{\varepsilon^2}{k} - R_\varepsilon$$

The model constants were set to the standard values of the RNG k-ε model: $C_{1\varepsilon} = 1.42$, $C_{2\varepsilon} = 1.68$, and $C_\mu = 0.0845$.

Notice that in the Fluent CFD software, the generation G_k of turbulence kinetic energy due to velocity gradients is expressed as function of the effective viscosity, $\mu_{\mathrm{eff}} = \mu + \mu_t$, rather than the pure turbulent viscosity, μ_t. This implementation (retained by Fluent for stability purposes in cases where G_k approaches zero) may not be suited to high temperature flows, as pointed out by Bolot and coauthors in (Ref 9). In the present case it results in a too short length of the plasma jet, as illustrated in Fig. 5a and b. The calculations of section 4 have thus been done subtracting the laminar viscosity contribution of G_k, as detailed in (Ref 10).

This system, supplemented by the boundary conditions specified below, was solved using a finite volume method and numerical schemes of second order accuracy in space.

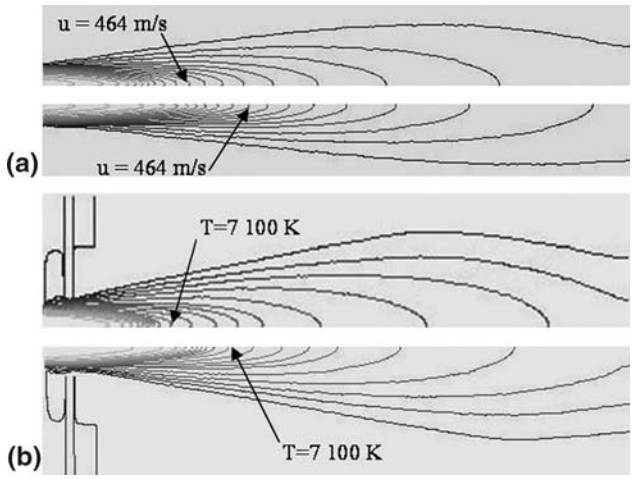

Fig. 5 (a) Velocity contours in a section along the plasma jet for test case B without plasma swirl. The half upper part was obtained with the RNG model as provided by Fluent; the half lower part was calculated using the correction of (Ref 9). (b) Temperature contours in a section along the plasma jet for test case B without plasma swirl. The half upper part was obtained with the RNG model as provided by Fluent; the half lower part was calculated using the correction of (Ref 9)

The boundary conditions at the nozzle exit (i.e., the inlet of the domain) were imposed time independent profiles of temperature, axial and swirl velocity, turbulence kinetic energy and dissipation rate. Turbulence kinetic energy and dissipation rate were modeled applying relations proposed by Bauchire (Ref 11). The following expressions were set for the normal velocity and temperature profiles:

$$u(r) = u_{\max}\left[1 - \left(\frac{r}{r_0}\right)^n\right]$$

with $n = 2$,

$$T(r) = (T_{\max} - T_{\mathrm{wall}})\left[1 - \left(\frac{r}{r_o}\right)^m\right] + T_{\mathrm{wall}}$$

with $m = 4.5$,

The maximum normal velocity $u_{\max}$ and maximum temperature $T_{\max}$ were derived as in (Ref 12) from the operating conditions of the arc generator (the torch voltage, arc current, and thermal efficiency given in Table 2) for a given swirl coefficient (defined as the ratio between the flux of angular momentum and the flux of axial momentum). Due to a lack of experimental data about the plasma swirl of test cases A and B, the swirl coefficient was set to the upper value of the range investigated in (Ref 13) that is $S_{\mathrm{swirl}} = 0.5$. The aim of this choice was to try to avoid underestimating the actual swirl. This parameter may indeed be important when investigating the effect (possible perturbation) of the gas screen (presented section 4.2.) on the plasma jet.

On the nozzle, ring, and powder injector walls, a no slip and constant temperature boundary condition was applied.

The surrounding air on the radial boundary of the computational domain was assumed to be at room temperature and at rest.

The substrate wall was replaced by a free boundary, as in the experiments (reported in section 5) done to measure inflight powder characteristics.

In the experimental setup, the cylindrical hose and pipe used for powder injection were respectively 5 m and 70 mm long. In the computational domain (of radius 25 mm) only a fraction of the pipe length (either 18 or 19 mm) was retained. For both test case A and B, the carrier gas flow rate and pipe diameter were associated with a Reynolds number larger than the critical Reynolds number of a flow in a smooth cylinder. A turbulent intensity of 10% was thus assumed at the inlet of the 70 mm pipe to calculate and interpolate the turbulent velocity profile needed at the pipe inlet of the computational domain. Notice that turbulence effects were most probably underestimated. The carrier gas was also assumed to be at room temperature.

3.3 Powder Model

The PM819-20 powder contains more than 90% of Zirconia and about 7% of Yttrine. Its properties (Table 5), needed for the numerical simulations, were

Table 5 Powder parameters

Powder	Ni-5wt.%Al	ZrO_2-7wt.%Y_2O_3
ρ_p, kg m^{-3}	8,590	5,400
c_p, J kg^{-1} K^{-1}	463	604
κ_p, W m^{-1} K^{-1}	98.3	2.3
T_{melt} (K)	1,686	2,950
Δh_{melt}, J kg^{-1}	302,765	710,000

considered similar to those of pure Zirconia (due to a lack of data concerning Yttrine). The PM 819-37 powder is mainly composed of Nickel and Aluminum (about 5%). Its properties (Table 5) were evaluated from the properties of these two components weighted by their respective mass fraction.

To avoid too heavy computational times, loading effects (Ref 14) were neglected although the powder flow rate was rather large (at least in test case B). The velocity and temperature of the particles were calculated with a Lagrangian approach (Ref 15-16) and taking into account the Reynolds dependence of the drag force, the variable property effects within the particle boundary layer, and gravity. Noncontinuum effects within the particle boundary layer, thermophoresis, and turbulent dispersion were also accounted for because of the presence of small particles (less than 20 or 10 μm). The temperature was assumed uniform inside the particles and the calculations did not account for evaporation or oxidation of the particles.

Although the particles had a numerical density rather large inside the pipe injector (at least in test case B) collisions between powder particles were neglected. Particle collisions with the pipe wall were modeled assuming partial momentum accommodation. A fraction of the particle-wall collisions were thus specular reflections while the rest was governed by diffuse reflection (of characteristic temperature the wall temperature). When colliding with either the nozzle or the ring wall, particles were supposed to be trapped, and afterwards no longer accounted for in the calculations. So particle aggregation in larger droplets, motion along the nozzle and ring walls under the action of gravity, and their possible loose as well, were not simulated. These ring and nozzle boundary condition were indeed simply aimed at easily detecting particle-wall collisions.

The initial conditions for the discrete phase were defined in an external file containing the injection distribution data for a set of 2,000 particles (the relevant particle data being here the position, velocity components, diameter and temperature). The number of particles per subset of given diameter was defined according to Table 3 (Table 4) for diameters larger than 45 μm, and based on the data of Fig. 3a (Fig. 3b) for diameters less than 45 μm.

4. Numerical Results

It has been observed (Ref 1) that lump formation occurs in production when the carrier gas flow rate is increased above some limit (from 2 to 4 slpm for test case A for instance) while keeping unchanged the other process parameters. An important step of the study was thus to check if a powder backflow could be detected via numerical calculations.

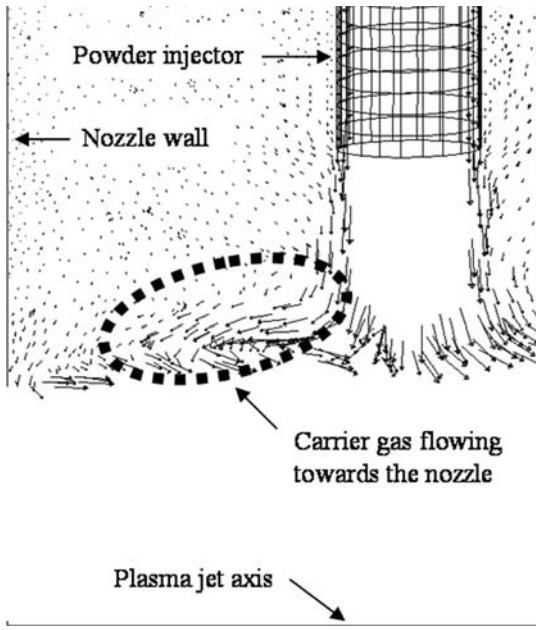

Fig. 6 Velocity vectors (calculated numerically with Fluent 6.1 for test case A) in the vicinity of the nozzle wall at the powder port outlet. Only vectors with norm less than 40 m/s are plotted

Simulations showed that at moderate flow rate (only 2 slpm in test case A for instance) the carrier gas only expands downstream: it is completely entrained along the direction of the plasma jet. At the larger rate given in Table 2, a small fraction of carrier gas flows backward, toward the nozzle wall (Fig. 6). Similarly, powder injection for a sufficiently large set of particles also showed a particle backflow (Fig. 7, top) and trapping at the nozzle wall (Fig. 7, bottom) when using large carrier gas flow rates. Calculation tests with (and without) either thermophoresis or turbulent dispersion also showed an increase (a reduction) in the amount of trapped particles. Accordingly, tests with a narrow range of particle diameters indicated that only particles of small diameter (about 10 μm and less) were entrained toward the nozzle.

4.1 Powder Port Location

Simulations, supplemented by experiments, have been performed in (Ref 2) to check if a change in powder port location had any effects on lump formation. Changes of small amplitude (up to 3 mm horizontal and/or vertical translation, also up to 5° tilting) resulted in some improvements: the carrier gas backflow was then slightly reduced. Similarly, the fraction of powder reaching the nozzle wall was also smaller. Changes of greater amplitude were needed to significantly reduce lump formation. However, these changes did not allow preserving the coating quality since the residence time of the powder particles into the plasma jet then gets too short. When

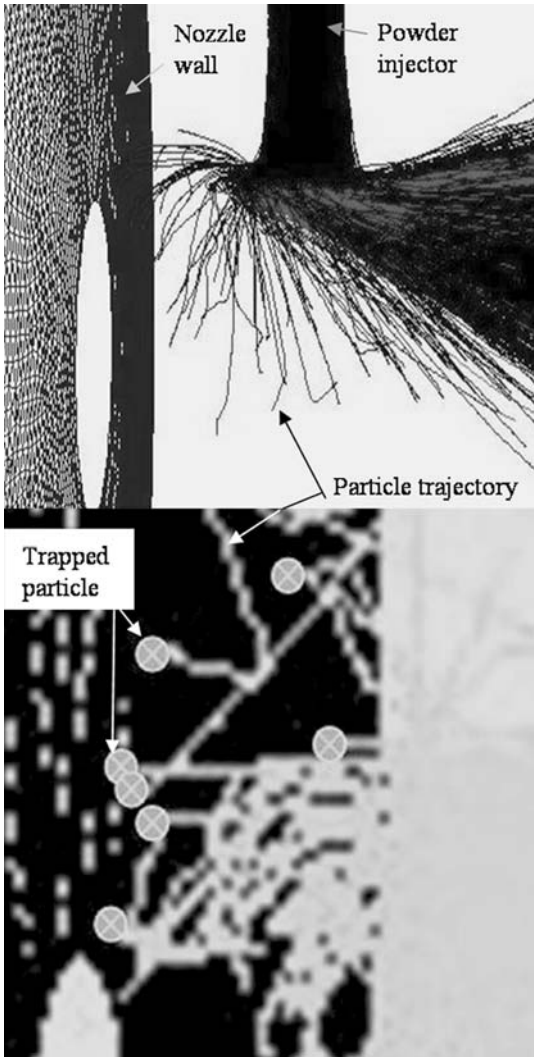

Fig. 7 Top: Particle trajectories (calculated numerically with Fluent 6.1, test case A) in the vicinity of the powder injector. Bottom: trapped particles (dots) on the nozzle wall (zoom, done for a larger set of particles)

tilting the pipe injector for instance, a minimum angle of 15° was needed to avoid clogging while a maximum angle of only 5° was allowed to maintain the coating properties. So this type of solution could not be justified.

4.2 Gas Screen

A way to prevent the backflow of powder from clogging the nozzle and forming lumps has been proposed in (Ref 2) and improved in (Ref 3). It consisted in applying a gas screen between the nozzle wall and the powder pipe injector, to divert from their path the particles flowing backward. To form this gas screen, the powder port ring holder fixed at the nozzle exit has been modified by milling grooves. Some constraints were imposed on the shape and size of the channels since it was decided to use the initial ring rather than designing a new one. When sealing the ring on the nozzle exit, the grooves resulted in channels. They

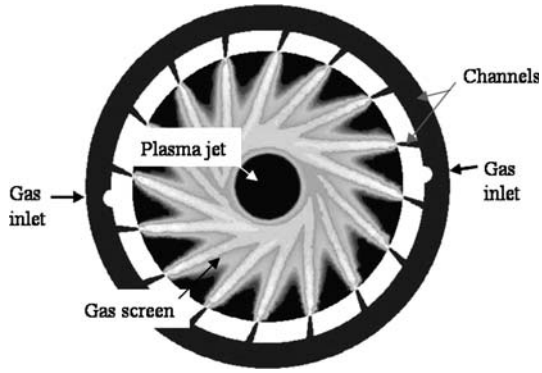

Fig. 8 Argon gas flowing through the circular ring channel and 16 triangular and convergent channels to form a screen at the nozzle wall (Fluent 6.2 calculation for test case 2, with 30 slpm total argon flow rate)

linked two pressurized gas screen inlets, via a circular channel of rectangular section (1 mm×3 mm), to 16 gas channels of triangular section (right isosceles of base 0.9 mm) opening on the inner radius of the ring (Ref 3). The 16 inner gas injection channels were evenly angularly distributed along the circumference of the ring. They were oriented along a nonradial direction, such that the injected gas could flow in the close vicinity of the outer periphery of the plasma jet, as illustrated in Fig. 8. Optimization of channels was discussed in (Ref 3), and is not reported here.

Notice that an important factor governing the efficiency of the protective gas layer is its evenness. This one is governed by the design of the channels (to reduce minor losses), the number of openings on the inner radius of the ring and the gas flow rate. Also, the gas screen must flow close enough to the plasma jet and be enough extended otherwise very small particles may cross it. These points were further detailed in (Ref 3). It was also observed numerically that a gas screen flowing toward the plasma jet, rather than around it, gets turbulent because of the screen-jet interaction, and thus inefficient. Thus the orientation of the triangular inner gas injection channels is also an important parameter for reaching screen efficiency.

4.3 Gas Screen Influence on the Plasma Jet

Although first aimed at preventing powder particles flowing backward from reaching the nozzle and ring walls, the gas screen could have secondary effects on the plasma jet and powder particles. It could indeed share some common features with the shroud gas flow investigated in (Ref 17). The gas screen had no velocity component along the plasma jet axis when formed, and it started forming far away from the jet. But its flow rate was rather large and it extended up to the close vicinity of the jet.

Test cases were calculated using a common mesh and (i) a swirling plasma jet without gas screen, (ii) a 30 slpm gas screen rotating around the swirling plasma jet along the same direction, and (iii) contrariwise. The isotherms and velocity contours are plotted for test case B in various sections along the jet axis: through the gas screen (Fig. 9a),

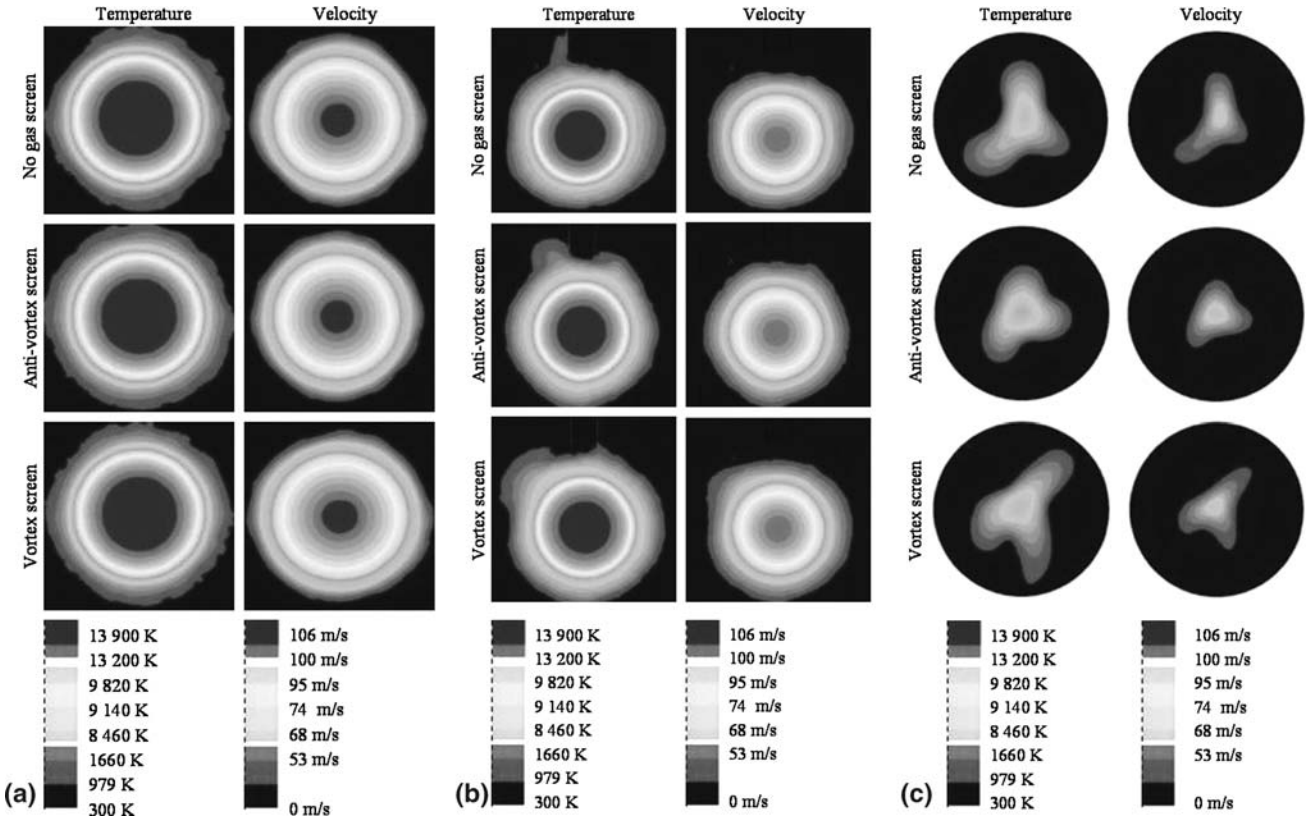

Fig. 9 Fluent 6.2 calculations, test case B. Plasma jet section at: (a) z = 0.5 mm (gas screen location), (b) z = 5 mm (powder injector location), and (c) z = 50 mm

through the powder injector (Fig. 9b), and further downstream (Fig. 9c).

No effect of the screen gas on the plasma jet was observed in the vicinity of the nozzle wall.

In the section of the powder injector, a very slight influence was noticed in the mixing layer at the periphery of the jet.

At 5 cm from the nozzle wall, the gas screen effect on the plasma jet was more pronounced, the shape of the jet and the isocontours were modified. For a screen gas flow opposing the plasma gas swirl, the plasma jet width was more uniform (with respect to the angular direction) and the calculated temperature and speed were slightly larger.

Plots along the jet axis, Fig. 10, 11, 12, show that the centre of the plasma jet was also modified by the presence of a gas screen. This effect was visible at about 2 cm from the nozzle exit and further downstream. For a screen gas flow and plasma gas swirl in the same direction, this effect was however very weak. For a screen gas flow opposing the plasma gas swirl component, a shroud effect was observed. The air engulfment in the plasma jet was then slightly reduced, and the jet length was increased by a few percent.

4.4 Gas Screen Influence on Powder Particles

A key issue was to maintain the coating properties. As underlined by Friis (Ref 18) and references within, the

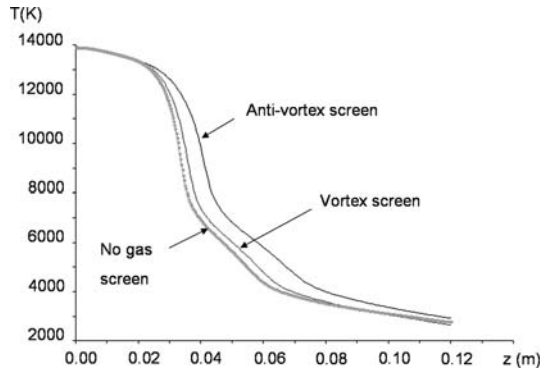

Fig. 10 Fluid temperature along the jet axis

characteristics of the powder particles prior to impact, such as velocity, temperature, also particle state (i.e., partly or fully molten) are very important factors influencing the microstructure and properties of the coating. It has been checked numerically (using sets of about 20,000 particles) that the average temperature and velocity of the powder particles, in a section perpendicular to the jet axis, were only very slightly changed (5% or less) when using either a 30 slpm vortex or a 30 slpm antivortex gas screen, or no gas screen. It has also been

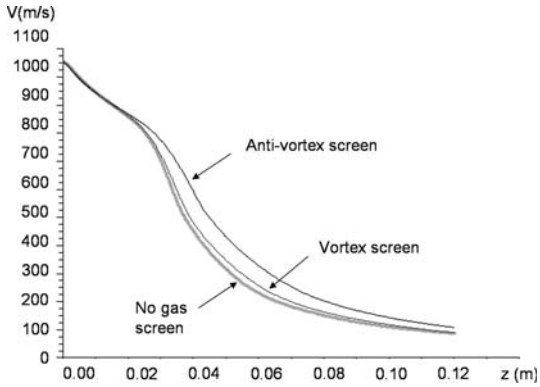

Fig. 11 Fluid velocity along the jet axis

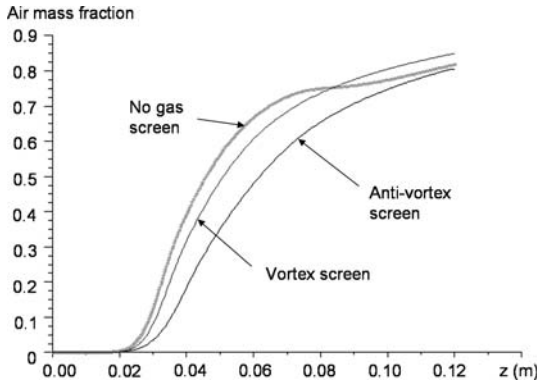

Fig. 12 Air mass fraction along the jet axis

observed that the standard deviations (associated with: the location of the particle jet mass center in a section, the velocity components and the temperature) were all lowered (resp. raised) when using an antivortex (resp. a vortex) gas screen instead of no gas screen. The effect was however rather weak: between 5 and 10% (depending on the variable). The vortex gas screen would thus tend to further disperse the particle jet, while the antivortex screen would tend to make it more focused. For a given set of injected particles, the size of the subset of particles reaching the substrate within the computational domain was significantly increased by an antivortex screen (by more than 10%) and reduced by a vortex screen (by about 10%). These observations are in agreement with the properties of the shroud and antivortex gas flows discussed in (Ref 17).

5. Experimental Results

Experiments were carried out for test case A and B, with and without gas screen. Different screen gas (argon or air), and different values of the screen gas flow rate through the ring (from 0 to 50 slpm) were tested. Various designs of the screen gas channels were also previously investigated (Ref 2-3). Only one relative orientation of the screen gas rotation with respect to the plasma swirl has been tested: the contrariwise one. Reported measurements were performed using rings with eight (test case A) and 16 (test case B) triangular channels for gas screen injection.

Table 6 Temperature and velocity of the powder particles on the jet axis and at substrate location (DPV2000 measurements)

Gas screen (slpm)	Test case A		Test case B	
	T, K	*u*, m/s	*T*, K	*u*, m/s
0	2,229	109	2,445	153
15	2,268	113	2,480	159
30	2,246	109	2,483	155
50	2,214	103	2,454	146

A simple inspection of the spray gun end piece after the spraying gave first indications. Clogging was observed in the absence of gas screen. In the presence of gas screen, the results depended on the flow rate of the pressurized gas used to form the protective layer. At low gas flow rate through the ring, such as 15 slpm, clogging was still observed but to a lesser extent (it took longer to appear compared to the case without screen). At higher rates, such as 30 and 50 slpm, there was no trace of powder clogged on the nozzle wall.

Diagnostics of inflight particles were carried out using the DVPS2000 system (Ref 19) by Tecnar Automation Ltée. This system is based on the detection of thermal radiation from the particles by an optical sensor located perpendicularly to the spray jet. It measures the velocity, surface temperature, and size of inflight particles in a measurement volume of 200 μm×300 μm×25 mm along the optical axis.

Measurements are reported in Table 6. They show a slight increase (less than 4%) in particle velocity and temperature when using a gas screen flow rate of 15 or 30 slpm rather than no screen. On the contrary, when further increasing the screen gas flow rate up to 50 slpm particle velocity and temperature start decreasing. Notice that a similar observation was done in (Ref 17) when investigating the effect of a shroud gas flow rate on a plasma jet length.

Cross-section grid measurements have also been made on (7×7) points with 5 mm spacing using the DVPS2000 system. Results obtained for test case B are plotted in Fig. 13 and 14. These figures also show a slight increase in particle velocity and temperature and decrease in dispersion when using 30 slpm gas screen rather than no screen. So the measurements indicate a small influence (only few percent) of the gas screen on the powder particles, that could result from the shroud effect on the plasma jet discussed section 4.3.

To analyze the microstructure of coatings obtained using the gas screen, titanium coupons were sprayed using the process parameters of test case A for the bond coat and test case B for the top coat. The optical microphotographs showed the presence of some lumps in the coatings for samples sprayed without gas screen and with 15 slpm

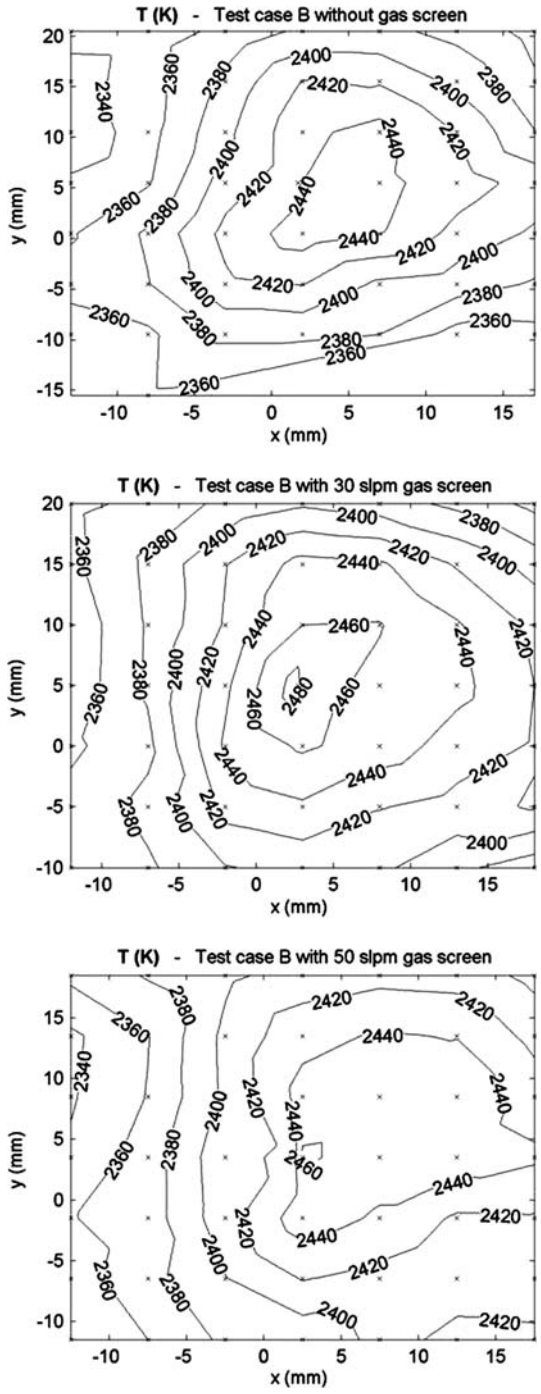

Fig. 13 Powder particle temperature at spray distance and in a section orthogonal to the plasma jet. Crosses represent experimental measurements. Isocontours were obtained by interpolation using Matlab

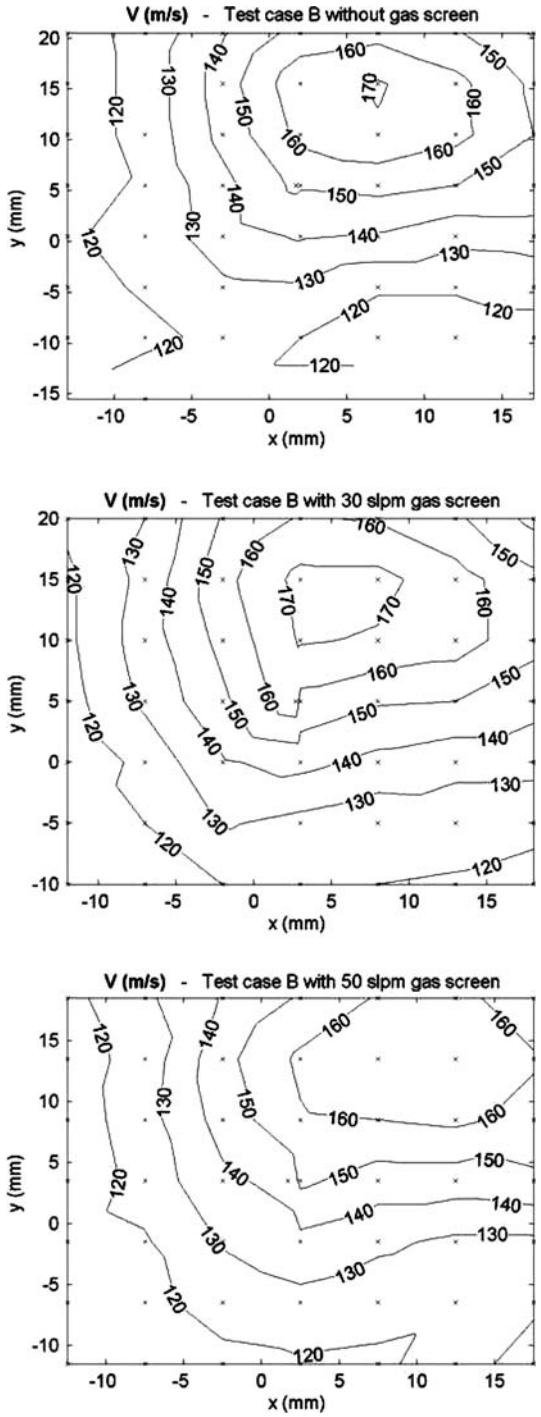

Fig. 14 Powder particle velocity at spray distance and in a section orthogonal to the plasma jet. Crosses represent experimental measurements. Isocontours were obtained by interpolation using Matlab

gas screen flow rate. No lump was observed when using a gas screen with a flow rate of 30 slpm or more to form the protective layer (Fig. 15 and 16).

Microscope image analysis was applied to evaluate the coating microstructure by comparison with reference photos (in specifications). The checked properties were the integrity between substrate and coating, the porosity, and the possible presence of cracks, delaminations, unmelts, and oxides. No difference was noticed when using a

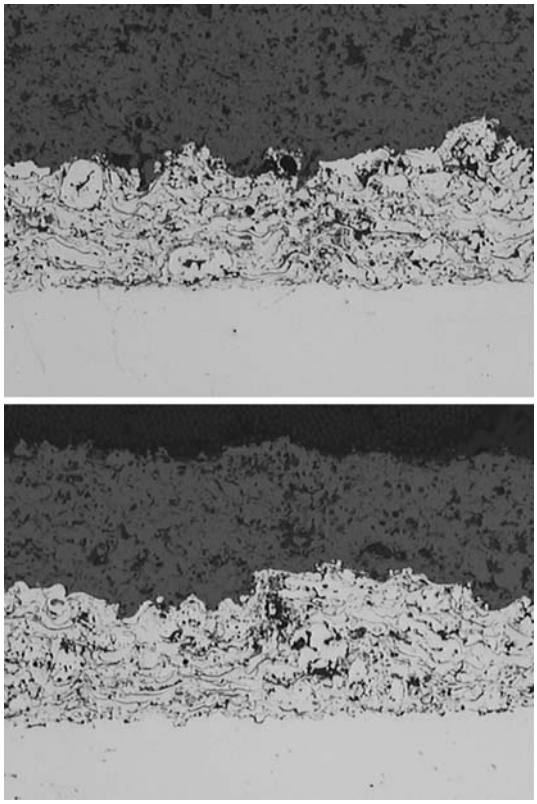

Fig. 15 Optical microphotographs; 833 × 625 μm. Microstructure for the coupons sprayed with: ordinary production parameters (top), 32 slpm Ar in the 8 channels ring (bottom)

protective gas layer of 30 slpm. The measured properties remained within the required quality range.

6. Conclusion

The proposed geometry of the powder port holder ring allows the formation of a flowing gas layer in the vicinity of the nozzle wall. When properly formed, this gas screen prevents powder back-stream from reaching the nozzle wall and thus from initiating lump formation in the coating. The efficiency of the proposed solution depends on the evenness of the injection points of the protective gas layer. To completely eliminate lump formation, a minimum number of injection channels, a proper orientation of these channels, and a minimum gas screen flow rate are needed.

When designed to form an antivortex flow this gas screen has some interesting secondary effects (shroud effects) on the plasma jet. Their repercussion on the powder particle characteristics prior to impact with the substrate are however weak. The important and related issue is to maintain the coating properties. Experiments showed that the coating quality was not affected by the presence of an antivortex gas screen during the spraying process.

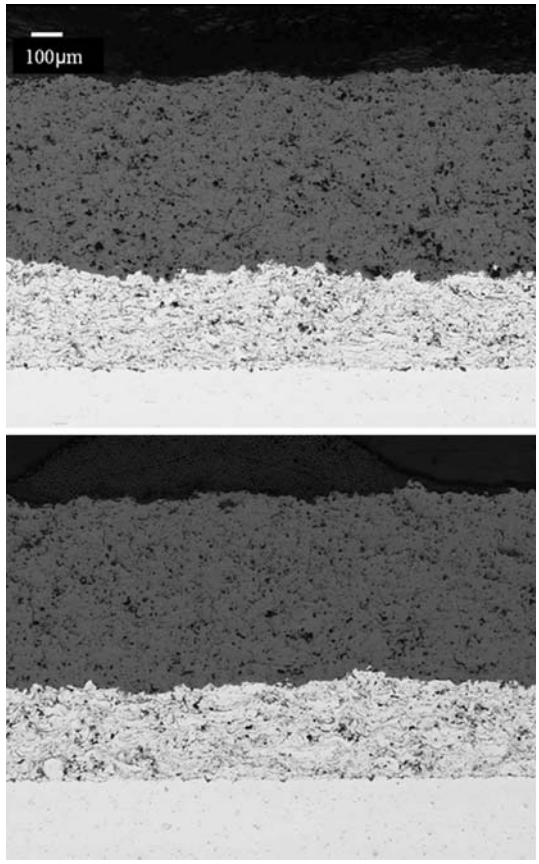

Fig. 16 Optical microphotographs. Microstructure for the coupons sprayed with: ordinary production parameters (top), 30 slpm Ar in the 16-channels ring (bottom)

Acknowledgments

The authors wish to acknowledge Mats-Olov Hansson, Carina Karlsson, Svante Magnusson, Peter Mårtensson, and Raymond Zakrisson, Volvo Aero Corporation, as well as Mats Högström and Fouzi Bahbou, University West, for their valuable contribution to the experimental investigations.

References

1. C. Langhammer, ''Optimisation of the deposition efficiency and deposition rate for PM 919-20 sprayed with the multi-local radial injection system,'' Report TC-02-227, Volvo Aero Corporation, 2002
2. I. Choquet, S. Björklund, J. Johansson, and J. Wigren, Nozzle exit geometry and lump formation in APS, International Thermal Spray Conference, E. Lugscheider, Ed., May 2-4, 2005 (Basel, Switzerland), DVS-Verlag GmbH, ISBN: 3-87155-793-5, 2005
3. I. Choquet, S. Björklund, J. Johansson, and J. Wigren, New powder port holder geometry to avoid lump formation in APS, 17th International Symposium on Plasma Chemistry, Ed. J. Mostaghimi, T.W. Coyle, V.A. Pershin, and H.R. Salimi Jazi, August 7-12, 2005 (Torronto, Canada), 2005
4. V. Kankanala and R. Kashani, ''Control modelling and regulation of thermal spraying process, Proceedings of the 6th National Thermal Spray Conference,'' Anaheim, CA, USA, 7-11 June 1993, C.C. Berndt, Ed., (Pub.) ASM International, OH, p 225-230 (1993)

5. E. Pfender, J. Fincke, and R. Spores, Entrainment of Cold Gas into Thermal Plasma Jets, *Plasma Chemistry and Plasma Processing*, 1991, **11**(4), p 529-543
6. J.R. Fincke and C.G. Pentecost, ''Laminar to turbulent transition and entrainment in thermal plasma jets, HTD-Vol161, Heat Transfer in Thermal Plasma Processing,'' *ASME*, 1991, p 101-106
7. J.O. Hinze, Turbulence, McGraw-Hill Publishing Co., New York, 1975
8. M.I. Boulos, P. Fauchais, and E. Pfender, Thermal plasmas: Fundamentals and Applications, Vol. 1, Plenum, New York, 1994
9. R. Bolot, J. Li, and C. Coddet, Modeling of thermal plasma jets: a comparison between PHEONICS and FLUENT, Proceedings of the International Thermal Spray Conference, ITSC 2004, Osaka, Japan, 10-12 May 2004, Thermal Spray Solutions: Advances in Technology and Application, ASM International, CD-Rom, ISBN: 0-87170-809-4, 2004, p 764-769
10. R. Bolot, J. Li, and C. Coddet, Some key advices for modeling of plasma jets using Fluent, Proceedings of the International Thermal Spray Conference, ITSC 2005, 2-4 May 2005, (Basel, Switzerland), DVS Verlag GmbH, Düsseldorf, Germany, CD-Rom, ISBN: 3-87155-793-5, 2005
11. J-M. Bauchire, Modélisation numérique d'une torche de projection à plasma : influence de la géométrie et de la turbulence sur les propriétés du plasma, PhD. Thesis, University Paul Sabatier, Toulouse, France, 1997
12. C.H. Chang and J.D. Ramshaw, Numerical Simulation of Argon Plasma Jets Flowing into Cold Air, *Plasma Chemistry and Plasma Processing*, 1993, **13**(2), p 189-209
13. S.A. Wurtzke, E. Pfender, and E.R.G. Eckert, Study of Electric Arc Behaviour with Superimposed Flow, *AIAA Journal*, 1967, **5**(4), p 707-717
14. A. Vardelle, M. Vardelle, P. Fauchais, P. Proulx, and M.I. Boulos, ''Loading effect by oxide powders in DC plasma jets,'' Proceedings of the 5th National Thermal Spray Conference, Orlando, FL, p 543-547 (1992)
15. A. Vardelle, M. Vardelle, K-I. Li, M. Vardelle, and P. Fauchais, ''Injection and trajectories of particles in D.C. plasma spray processes, Proceeding of the 12th International Symposium on Plasma Chemistry,'' 21-25 August 1995, Minneapolis, MN, USA, J.V. Heberlein, T.W. Ernie, J.T. Roberts, Ed, p 1343-1348 (1995)
16. P. Nylén, The prediction of Fluid flow, particle in-flight and coating characteristics in atmospheric plasma spraying, PhD thesis, Chalmers University, Sweden, 1999
17. H.C. Chen, Z. Duan, J. Heberlein, and E. Pfender, ''Influence of shroud gas flow and swirl magnitude on arc stability and coating quality in plasma spray,'' Thermal Spray: Practical Solution for Engineering Problems, C.C. Berndt, Ed., (pub.) ASM International, Materials Park, OH, USA, 1996, p 553-561
18. M. Friis, A methodology to control the microstructure of plasma sprayed coatings, PhD thesis, Lund University, Sweden, 2002
19. C. Moreau, P. Gougeon, M. Lamontagne, V. Lacasse, G. Vaudreuil, and P. Cielo, On-line control of plasma spraying process by monitoring the temperature, velocity, and trajectory of in-flight particles, Thermal Spray: Industrial Applications, 1994, p 431-437